Journal of Alloys and Compounds 886 (2021) 161268

Contents lists available at ScienceDirect

Journal of Alloys and Compounds

journal homepage: www.elsevier.com/locate/jalcom

Destroying the symmetric structure to promote phase transition: Improving the SERS performance and catalytic activity of MoS_2 nanoflowers

Rui Su[a,b,c], Yingnan Quan[c,d,e], Shuo Yang[f], Mingyue Hu[c,d,e], Jinghai Yang[c,d,e,*], Ming Gao[c,d,e,*]

[a] Changchun Institute of Optics, Fine Mechanics and Physics, Chinese Academy of Sciences, Changchun 130033, PR China
[b] University of Chinese Academy of Sciences, Beijing 100049, PR China
[c] Key Laboratory of Functional Materials Physics and Chemistry of the Ministry of Education, Jilin Normal University, Changchun 130103, PR China
[d] National Demonstration Centre for Experimental Physics Education, Jilin Normal University, Siping 136000, PR China
[e] Key Laboratory of Preparation and Application of Environmental Friendly Materials, Jilin Normal University, Ministry of Education, Changchun 130103, PR China
[f] College of Science, Changchun University, Changchun 130022, PR China

ARTICLE INFO

Article history:
Received 14 June 2021
Received in revised form 13 July 2021
Accepted 19 July 2021
Available online 22 July 2021

Keywords:
Ni-doped MoS_2
SERS
Enhancement mechanism
Trace detection
Catalytic activity

ABSTRACT

Semiconductor surface-enhanced Raman scattering (SERS) substrates with excellent stability and uniformity have attracted more and more attention and can theoretically address deficiencies of noble metal. However, a key problem ahead of practical is how to improve sensitivity. Here, we introduce a metal-free, Ni-doped MoS_2 nanoflowers (NFs) as SERS substrates with a significant enhancement factor of 3.56×10^5. This remarkable enhancement is attributed to three factors: (1) 1 T-2 H mixed-phase provides more electrons, significantly improved the charge transfer process and electromagnetic enhancement; (2) Ni doping improves the polarity of MoS_2 NFs and enhances the interface dipole-dipole interaction with MB molecules; (3) increases the specific surface area of MoS_2 NFs enabled sufficient interaction with the Methylene blue (MB) molecules. The Ni-doped MoS_2 NFs was used to detect pollutants such as bilirubin, which shows super sensitive SERS activity with the detection limit as low as 10^{-7} M. Moreover, this substrate has excellent stability and uniformity. Importantly, Ni doped MoS_2 NFs also exhibits excellent catalytic activity. We believe that this research will not only help promote the application of MoS_2 NFs for biosensor application but also provide help for understanding the enhancement mechanism of semiconductors as SERS substrates.

1. Introduction

Surface enhanced Raman spectroscopy (SERS), as a potent and powerful real-time surface analysis technology [1–4], has unique advantages such as non-destructive, single-molecule level detection sensitivity and molecular specificity, which has been widely used in environmental monitoring [5–7], biosensing [8–10] and food safety [11–14]. At present, the main mechanisms of SERS are electromagnetic enhancement (EM) and chemical enhancement (CM) [15]. EM is related to the Local surface plasmon resonance (LSPR) on the metal surface [16–19]. The LSPR effect can greatly increase the Raman signal of the molecule. Therefore, metal materials are the most important substrate materials on SERS research. However, it is not complete to explain the SERS phenomenon only through EM. For example, the ability of the substrate to adsorb target molecules is positively correlated with the performance of SERS. This is due to charge transfer between the substrate and the molecule [20,21]. The reason for these phenomena can be attributed to CM. At the same time, metal substrates also have some inherent disadvantages such as complex synthesis process, high cost, poor stability and biocompatibility [22]. Hence, the top priority is to discover new materials that can replace precious metals.

Semiconductors have been manifested have the potential to displace metal materials as reliable SERS substrates [23]. Two-dimensional (2D) transition metal dichalcogenides (TMDs) have been universally concerned account of their unique qualities in multiple application fields, such as catalysis [24,25], field-effect transistors [26,27], and photodetectors [28]. Among TMD materials, molybdenum disulfide (MoS_2) is the most extensively explored one,

* Corresponding authors at: Key Laboratory of Functional Materials Physics and Chemistry of the Ministry of Education, Jilin Normal University, Changchun 130103, PR China.
E-mail addresses: jhyang1@jlnu.edu.cn (J. Yang), gaomingphy@126.com (M. Gao).

https://doi.org/10.1016/j.jallcom.2021.161268
0925-8388/

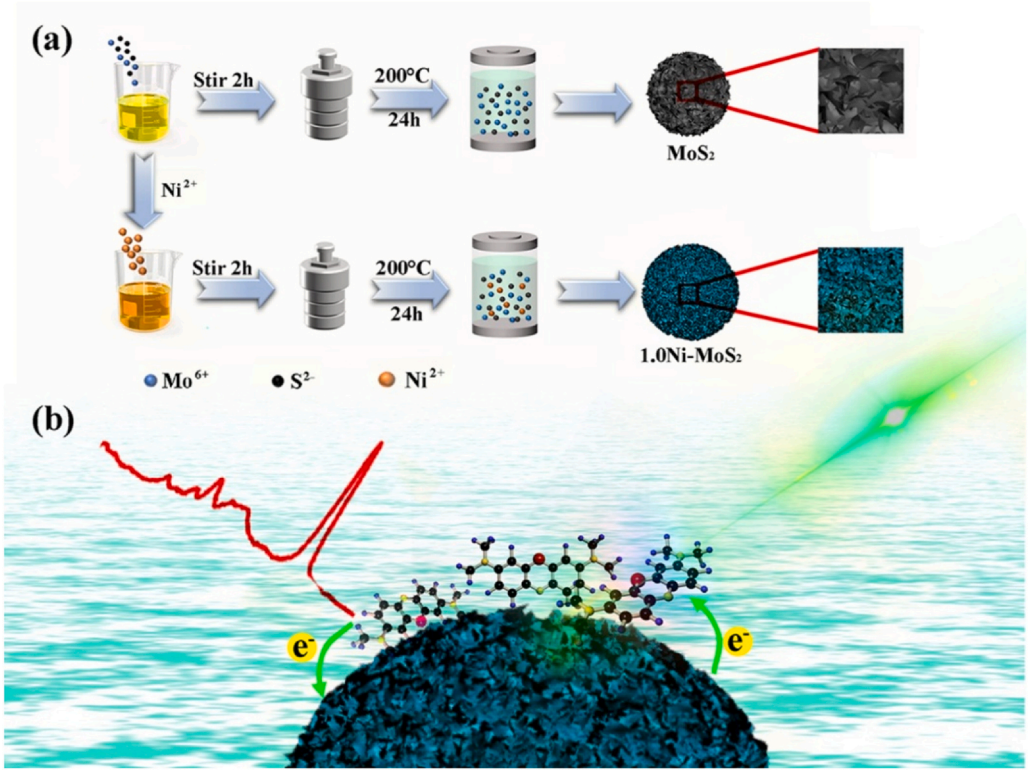

Fig. 1. (a) Illustrative representation for the synthesis of MoS_2 NFs and Ni–MoS_2 NFs samples. (b) Simulation diagram of SERS measurement.

with large reserves, low cost and high carrier mobility [29,30]. At the same time, MoS_2 also has two characteristic phases: semiconductor 2H phase and metal 1 T phase. The 1 T phase has high conductivity and electronic density of states, which not only promotes charge transfer between the substrate and molecules, but also effectively reduces the recombination of electron and hole, and is expected to become one of the candidate materials for SERS substrates [31–34]. However, the carrier concentration of pure MoS_2 is low, pure MoS_2 has a three-atom layer symmetric structure of S–Mo–S, and its polarity is weak. Its enhancement effect is only about two orders of magnitude [35], which severely restricts its practical application.

Currently, more and more studies have been given priority to promoting the poor SERS performance of MoS_2 substrates [36]. Such as, some have combined noble metal nanoparticles with MoS_2, since there are advantages like high physical enhancement in noble metals. Liang et al. prepared a 3D MoS_2-NS @Ag-NP composite material and used this material as a SERS substrate, and the enhancement factor (EF) as high as 1.2×10^8 [37]. However, the substrate is not stable due to the presence of precious metals, so the synthesis of stable and high SERS performance substrate is still a significant challenge. Besides, the doping of oxygen atoms in the semiconductor will effectively improve the enhanced performance of the semiconductor SERS substrate. Zheng et al. doped molybdenum disulfide with oxygen atoms. Compared with pure molybdenum disulfide, its enhancement factor is increased by 10^6 times and the lowest detection limit for R6G can reach 10^{-7} M [22]. Doping is often used as a means of modifying materials. It can replace atoms in MoS_2 or dope heteroatoms into lattice gaps, which increases the number of defects in MoS_2, breaks the three-atom symmetry structure of MoS_2, and improves the polarity of MoS_2. Therefore, we choose doping to modify the material, improving the polarity of the material, adjusting its carrier concentration, changing its electronic energy band structure, and enhancing its photoelectric performance [38,39]. The transition metal element Ni is cheap and environmentally friendly, and the radius of Ni^{2+} ions (r = 0.69 Å) is slightly larger than the radius of Mo^{4+} ions (r = 0.65 Å), which is beneficial to the doping of MoS_2 [40].

In this paper, Ni-doped MoS_2 nanoflowers (Ni–MoS_2 NFs) are synthesized by hydrothermal method, and the SERS performance of Ni–MoS_2 NFs is optimized by adjusting the doping concentration. The results show that the synthesized 1.0Ni-MoS_2 NFs has the best SERS performance, and the enhancement mechanism of the 1.0Ni-MoS_2-MB system was systematically analyzed in detail. Destroying the structure of MoS_2 leads to an increase in polarity, the appearance of 1 T phase MoS_2 and Ni doping increase the defects and carrier concentration of MoS_2 NFs, which are the reasons for the excellent SERS performance of 1.0Ni–MoS_2 NFs. And 1.0Ni–MoS2 NFs as a SERS substrate has good stability, repeatability and high sensitivity to bilirubin. Furthermore, the catalytic performance of the doped MoS_2 NFs is also greatly improved. Compared with pure MoS_2 NFs, its catalytic performance for MB increased by 46.73%.

2. Results and discussion

2.1. Structure and morphology of MoS_2 NFs and Ni-MoS_2 NFs

As shown in Fig. 1a, MoS_2 NFs and Ni-MoS_2 NFs were prepared via a hydrothermal process and linked to probe molecule as SERS substrates (See supporting information for experimental details).

The XRD patterns of MoS_2 NFs, 1.0Ni–MoS_2 NFs, and 2.0Ni–MoS_2 NFs are shown in Fig. 2a. All main characteristic peaks in 1.0Ni–MoS_2 NFs are precisely matched according to MoS_2 NFs as reported in the JCPDS card (no. 37-1492). The results illustrate that for 1.0Ni-MoS_2 NFs, the MoS_2 NFs crystal structure is completely retained after doping of Ni, indicating that doping did not destroy the main structure of MoS_2 NFs [41]. The dominant peaks of 17.479°, 32.649° and 56.825° are assigned to the (002), (100), and (110) crystal planes of the pure MoS_2 NFs [30,42]. The (002) diffraction peak indicates that MoS_2 NFs forms a good stacked layer structure during the hydrothermal process. In addition, the solubility of Ni ions in MoS_2 NFs

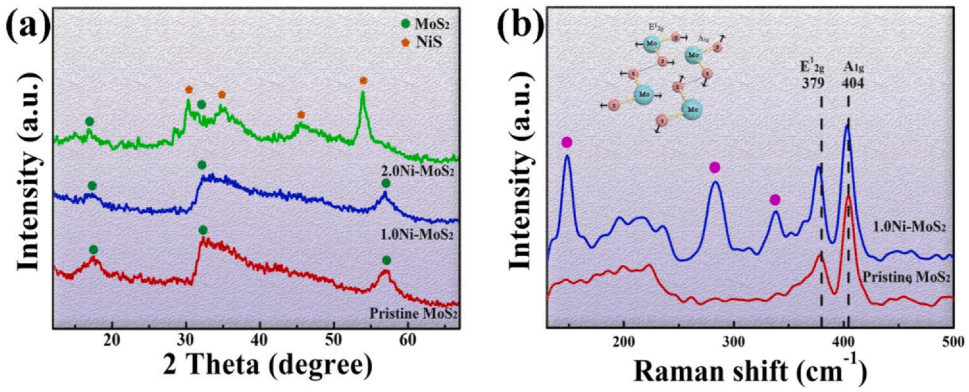

Fig. 2. (a) XRD patterns of the pristine MoS_2 NFs, 1.0Ni-MoS_2 NFs, 2.0Ni-MoS_2 NFs. (b) Raman spectra of MoS_2 NFs, 1.0Ni-MoS_2 NFs (the inset is A_{1g} and E^1_{2g} Raman vibration modes).

is limited. The XRD spectrum of 2.0Ni-MoS_2 NFs shows that excess Ni ions react with S ions to form NiS precipitation (JCPDS card number 02-1280) [43]. This shows that when the doping concentration is too high, the hydrothermal reaction generates NiS/MoS_2 composite materials. However, this thesis mainly studies the influence of doping on the SERS and catalytic performance of MoS_2 NFs and the mechanism analysis, so the following will mainly analyze pure MoS_2 NFs and 1.0Ni-MoS_2 NFs. Raman spectra were used to further explore the crystal structure of pure MoS_2 NFs and 1.0Ni-MoS_2 NFs in Fig. 2b. The pure MoS_2 NFs and 1.0Ni-MoS_2 NFs show two characteristic peaks at 379 and 404 cm^{-1}, which are consistent with the E^1_{2g} and A_{1g} modes of the hexagonal MoS_2 NFs crystal [43,44]. The vibration peak of E^1_{2g} is related to plane vibration, while the peak of A_{1g} represents the vibration along the out-of-plane direction of the sulfide (the inset of Fig. 2b). After Ni-doping, the frequency of the E^1_{2g} and A_{1g} are slightly red shifted due to the new interaction weakening the Mo-S bond vibration [45,46]. Besides, this shift also indicates the strain has changed in MoS_2 NFs and weaken the relative action between two adjacent MoS_2 NFs layers, which will cause a change in appearance [47]. Interestingly, in the Raman image of 1.0Ni-MoS_2 NFs, new Raman peaks (marked by purple circles) appeared at 148, 286, and 337 cm^{-1}. The existence of these peaks confirmed the formation of 1 T MoS_2 [41].

XPS spectra show the chemical composition and status of pure MoS_2 NFs and 1.0Ni-MoS_2 NFs. In the XPS spectrum of 1.0Ni-MoS_2 NFs, Mo, S and Ni peaks can be clearly identified (Fig. 3a). For pure MoS_2 NFs, the peaks at 228.88 eV and 232.04 eV are attributed to Mo $3d_{5/2}$ and Mo $3d_{3/2}$ core levels (Fig. 3b), respectively. While for 1.0Ni-MoS_2 NFs, they shifted ~0.30 eV towards the higher binding energy than pure MoS_2 NFs due to the Ni^{2+} ions doping and the electronegativity of Ni^{2+} is higher than that of Mo^{4+} [43]. A small low-energy peak was found at 226.18 eV, which was attributed to the S 2 s orbital of sulfide ion. For the S 2p XPS spectra of pure MoS_2 NFs and 1.0Ni-MoS_2 NFs (Fig. 3c), the binding energies of S 2p is 161.77 eV and 163.00 eV [48]. At the same time, compared with pure MoS_2 NFs, the S 2p peak in 1.0 Ni-MoS_2 NFs is also found to move in the same

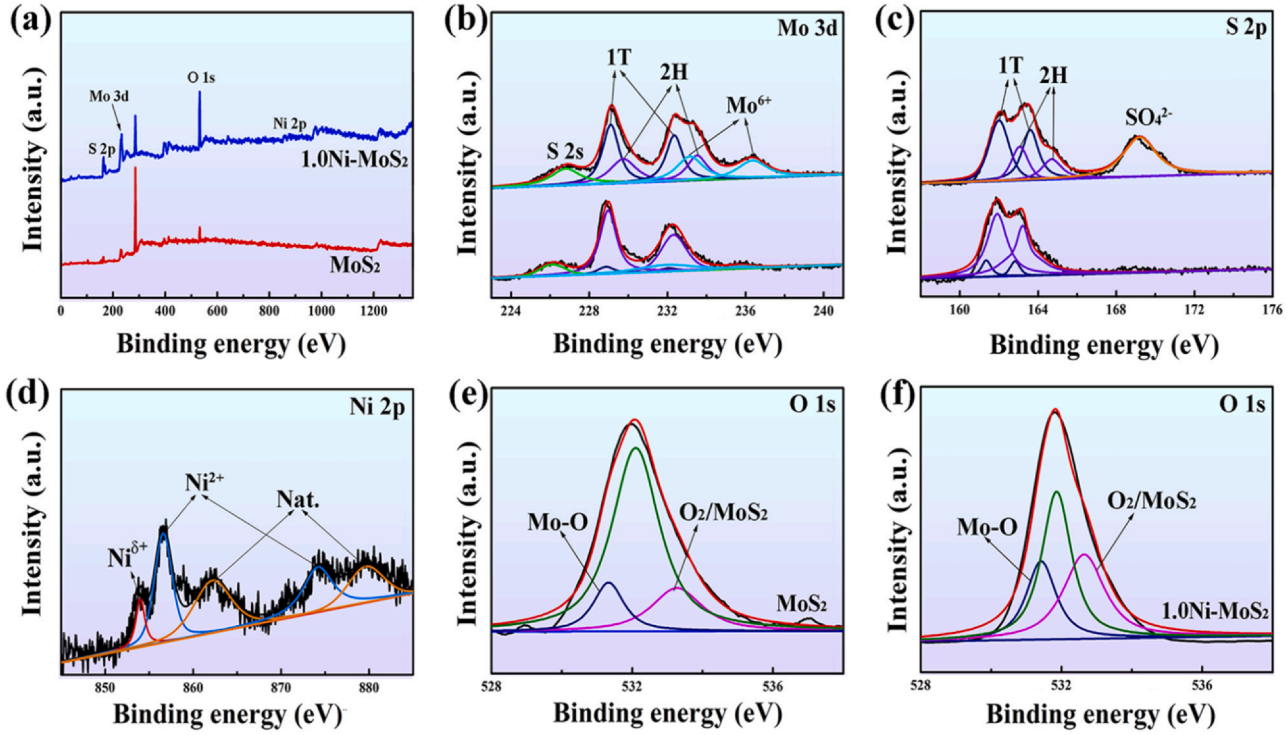

Fig. 3. (a) XPS total spectrum of MoS_2 NFs and 1.0Ni–MoS_2 NFs. High-resolution XPS spectra of (b) Mo 3d, (c) S 2p, and (d) Ni 2p of the 1.0Ni–MoS_2 NFs, pristine MoS_2 NFs. XPS spectra of O 1 s of (e) the pristine MoS_2 NFs, (f) the 1.0Ni–MoS_2 NFs.

trend as the Mo 3d peak. A characteristic peak at 856.60 eV can be greatly observed in the XPS spectrum of the high-resolution Ni 2p state of 1.0Ni-MoS_2 NFs, which is related to the Ni^{2+} $2p_{3/2}$ orbital (Fig. 3d) [43]. No characteristic peaks are observed in the XPS spectrum of pure MoS_2 NFs with the same binding energy. The typical Ni 2 P spectrum could be well fitted. The double peak at 862.20 eV and 879.87 eV are attributed to satellite peak. It is attributable to $Ni^{\delta+}$ at the binding energy of 854.00 eV (δ is the value close to 0). The existence of this peak proves that Ni forms the Ni-S-Mo bond in MoS_2 NFs [49]. In addition, Fig. 3d shows the Ni 2p core energy level spectrum, which can also directly prove the Ni dopant forms a bond with Mo and S in 1.0Ni-MoS_2 NFs. In addition, the known Mo 3d spectrum was fitted, and two binding energy peaks corresponding were found at 232.22 eV and 235.80 eV, which were attributed to the binding energy peaks of the Mo^{6+} 3d core energy level. This is mainly due to the incomplete sulfidation during the hydrothermal synthesis process [25]. Similarly, fitting the S 2p spectrum, the binding energy peak at 169.40 eV is attributed to SO_4^{2-}, and the existence of the S-O bond is due to a small amount of sulfate residues in the sample [49]. In addition, there are other peaks in the Mo 3d region and S 2p region. These additional peaks indicate that not only the semiconductor 2 H phase but also the metal 1 T phase exists in MoS_2 NFs and 1.0 Ni-MoS_2 NFs [31,50–52]. After calculation, the 1 T phase content increased from 6.75% in pure MoS_2 NFs to 43.12% in 1.0Ni-MoS_2 NFs. It can be found that for MoS_2 NFs, doping can greatly increase the metal 1 T phase. This is the same as the intrinsic Raman results. It can be seen from the XPS spectrum of Mo that the content of Mo^{6+} increases significantly, which is mainly due to the interaction between Mo and O to form a Mo-O bond. It is found through XPS total spectrum that the O content in pure MoS_2 NFs is lower than the O content in 1.0Ni-MoS_2 NFs. In Fig. 3e-f, the XPS spectrum of O 1 s core levels are fitted, and the peaks at 533.26 eV, 532.09 eV, and 531.32 eV are derived from O_2/MoS_2, O bond, and Mo-O bond [53]. The existence of O_2/MoS_2 and Mo-O indicates that MoS_2 NFs has both physical and chemical adsorption capabilities for O. In order to show the changes of Mo and O more intuitively, through calculation, the detailed percentage content of Mo^{6+} in the total amount of molybdenum and the detailed percentage content of Mo-O and O_2/MoS_2 in the total amount of oxygen are obtained (See Table S1). Compared with MoS_2 NFs, the Mo^{6+} content in 1.0Ni-MoS_2 NFs has increased, due to the formation of more Mo-O bonds after Ni-doped MoS_2 NFs. It can be calculated that 1.0Ni-MoS_2 NFs can adsorb more oxygen atoms than pure MoS_2 NFs, and the number of Mo-O bonds is also greater than that of pure MoS_2 NFs. Indicate that more oxygen atoms are physically and chemically adsorbed on 1.0Ni-MoS_2 NFs, which indicates that the ability of 1.0Ni-MoS_2 NFs to adsorb foreign molecules is enhanced.

The morphology of the pure MoS_2 NFs and 1.0Ni-MoS_2 NFs were investigated by SEM and TEM. The uniform flower-like architecture of MoS_2 clusters with a diameter of about 300 nm are obtained by hydrothermal method (Fig. 4a and Fig. S1a). And petal like MoS_2 sheets are well assembled together from high-magnification SEM image (inset of the Fig. 4a), exhibiting a clear multilayered structure. This is particularly interesting because there are some groups such as -SH, $-NH_2$, COO^- in L-cysteine, and these groups can be combined with metal ions and other functional groups. Therefore, during the reaction, L-cysteine is not only a reduction agent, but also a source of sulfur in MoS_2 NFs. L-cysteine releases H_2S, reducing the MoO_4^{2-} precursor in $Na_2MoO_4{\cdot}H_2O$ to MoS_2 NFs. The synthetic process of MoS_2 NFs can be expressed by Eqs. (1, 2 and 3).

$$9HSCH_2CHNH_2COOH + 9H_2O \rightarrow 9CH_3COCOOH + 9NH_3 + 9H_2S \quad (1)$$

$$4MoO_4^{2-} + H_2S + 6CHCOCOOH \rightarrow 4MoO_2 + SO_4^{2-} + 6CHCOCOO- + 4H_2O \quad (2)$$

$$4MoO_2 + 8H_2S \rightarrow 4MoS_2 + 8H_2O \quad (3)$$

In the course of the stirring process after blending $Na_2MoO_4.2H_2O$ and L-cysteine, the blended solution becomes transparent. This may be due to the combination of the hexavalent molybdenum ion and the side chain of L-cysteine to form a Mo $(Cys)^{6+}$ complex. After heating, the complexes would decompose, thereby producing Mo^{6+} and L-cysteine. Then, the strong nucleophilic O atom of the H_2O molecules attacks L-cysteine and slowly releases the S^{2-} anion. At the same time, Mo^{6+} cation is reduced by

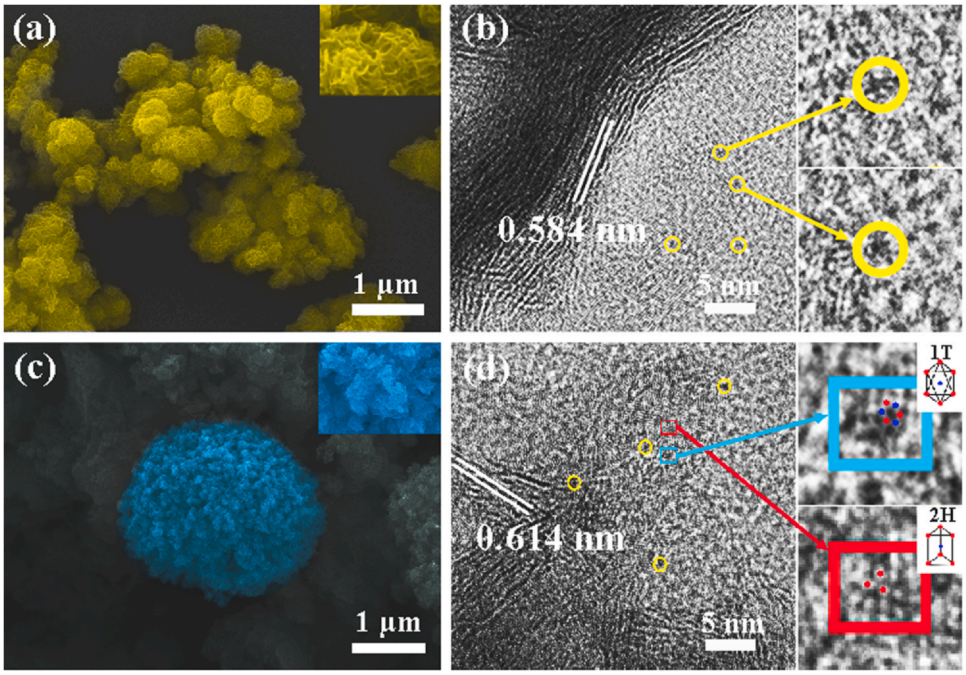

Fig. 4. (a) SEM image of MoS_2 NFs (inset is a partial enlarged view); (b) TEM image of MoS_2 NFs (yellow circle is enlarged on the right side of the (b) figure, and the circle represents a defect); (c) 1.0Ni–MoS_2 NFs SEM Image (inset is a partial enlarged view); (d) TEM image of 1.0Ni–MoS_2 NFs (on the right side of the figure (d), the red area and blue area are respectively enlarged, the red area is the lattice arrangement of 1 T phase MoS_2 NFs, the blue area is the lattice arrangement of 2H phase MoS_2 NFs).

S^{2-} anion to MoO_2. Then, the remaining S^{2-} reacts with MoO_2, and the final product is MoS_2 NFs. In addition, the amino group at one end of the L-cysteine molecule can react with the carboxyl group at the other end to form dipeptides or polymorphisms and provide a template for the growth of molybdenum disulfide nanoflowers [54,55]. The SEM image of 1.0Ni–MoS_2 NFs is shown in Fig. 4c and Fig. S1b. Due to the increase number of defects after Ni atom doping, the layer-to-layer interaction is weak, so the MoS_2 NFs are separated into small nanoflowers [56]. However due to the magnetism of Ni, these small nanoflowers agglomerate and form larger clusters [39].

The HRTEM images of pure MoS_2 NFs and 1.0Ni–MoS_2 NFs are shown in Fig. 4b and d. Through measurement, it is found that the (002) interlayer spacing of 1.0Ni-MoS_2 NFs is 0.614 nm, which is greater than the MoS_2 NFs (002) interlayer spacing of 0.584 nm. The atomic ratio in the sample can be obtained by XPS test (Table S2). According to the proportions of Mo, Ni and S, it can be obtained that Ni replaces Mo atoms during the doping process. The doping of Ni ions with a larger radius causes the lattice to expand, thereby increasing the MoS_2 NFs layer spacing [57]. The yellow circle in the figure shows the typical defects of the material (the illustration shows a larger view of the yellow circle). It is obvious that there are more defects in 1.0Ni–MoS_2 NFs than pure MoS_2 NFs. In addition, HRTEM image of the 1.0Ni–MoS_2 NFs also shows the lattice fringe of the basal plane with both 1 T and 2H phases. The red area and blue area in Fig. 4d are further enlarged. The symmetrical arrangement of the octahedral phase sulfur atoms and molybdenum can be observed in the blue region, which belongs to the characteristic structure of 1 T phase MoS_2 NFs. The red region has a structure surrounded by a symmetric Mo-Mo spacer region by three S atoms, which is a typical structure of 2H phase MoS_2 NFs [42]. This is consistent with the conclusion of Raman results. At the same time, the lower magnification TEM images of MoS_2 NFs and 1.0Ni–MoS_2 NFs are shown in Fig. S2. It can be obtained from the Fig. S2 that the pure MoS_2 nanoflower petals have obvious layered structure and thicker petals. The 1.0Ni-MoS_2 nanoflower petals have a thinner layered structure and more diverse growth directions, which may generate more active sites. The reason for this phenomenon can be attributed to the destruction of the layered structure of MoS_2 NFs by Ni doping.

2.2. SERS activity of Ni–MoS_2 NFs

In order to evaluate the SERS performance of the synthesized samples, SERS detection was carried out on MB molecules (10^{-3} M). The results showed that the SERS performance of different samples is quite different. Table S3 lists the positions of the intrinsic Raman peaks of the MB molecules, and assigns the vibration modes of the MB molecules to the imperfectly symmetrical mode (E) and the fully symmetrical mode (A1), respectively. The SERS spectra of MoS_2 NFs, 1.0Ni–MoS_2 NFs and 2.0Ni–MoS_2 NFs were collected in Fig. 5a. To clearly show the change of intensity relative to the doping Ni concentration, the SERS intensity of 1625 cm^{-1} was plotted (Fig. 5b). It can be found from the MB characteristic peak at 1625 cm^{-1} that 1.0Ni-MoS_2 NFs was used as the substrate, the SERS enhanced performance was the best. Fig. 5c further magnifies the peak at 1625 cm^{-1}. It is found that compared with other Raman peaks, with 1.0Ni-MoS_2 NFs as the substrate, the MB molecule moves the most to the right. This is because charge transfer between MB molecules and 1.0Ni-MoS_2 NFs substrate is stronger than that between MB molecules and other substrates [58]. In order to reflect the SERS performance of 1.0Ni–MoS_2 NFs, the enhancement factor of the 1.0Ni–MoS_2 sample is calculated, and the final result is 3.56×10^5 (the detailed calculation process is in Supplementary Note 1) [59]. And we also measured the Raman signal of MB molecules when 2.0Ni–MoS_2 NFs was used as the substrate, and the results showed that the SERS performance of the 2.0Ni-MoS_2 NFs substrate was lower than that of the 1.0Ni-MoS_2 NFs substrate. This is because the precipitated NiS impurities adhere to the surface of MoS_2 NFs and hinder the contact between the molecules and MoS_2 NFs, thus reducing the SERS performance of MoS_2 NFs.

2.3. SERS enhancement mechanism of Ni–MoS_2 NFs

Generally, CM enhancement is a main contribution to the SERS effect as for most semiconductors. According to the Herzberg-Teller vibronic coupling mechanism, the charge transfer effect can lead to an increase in the strength of the non-totally symmetric modes of the molecule [60]. Therefore, the SERS intensity of the MB molecule non-totally symmetric modes on 1.0Ni-MoS_2 NFs was studied, and the contribution of charge transfer (CT) in the SERS system was further evaluated. So, the vibration mode of the MB molecule needs to be determined. According to Table S3, the vibration mode of the MB molecule is determined, the non-totally symmetric modes at 672 cm^{-1} and the totally symmetric modes at 770 cm^{-1} are selected to evaluate the charge transfer degree of the 1.0Ni–MoS_2 NFs substrate (Fig. 5a).

The degree of charge transfer (ρ_{CT}) can be known by the formula:

$$\rho_{CT} = \frac{I_{ntsm}/I_{tsm}}{1 + (I_{ntsm}/I_{tsm})} \quad (4)$$

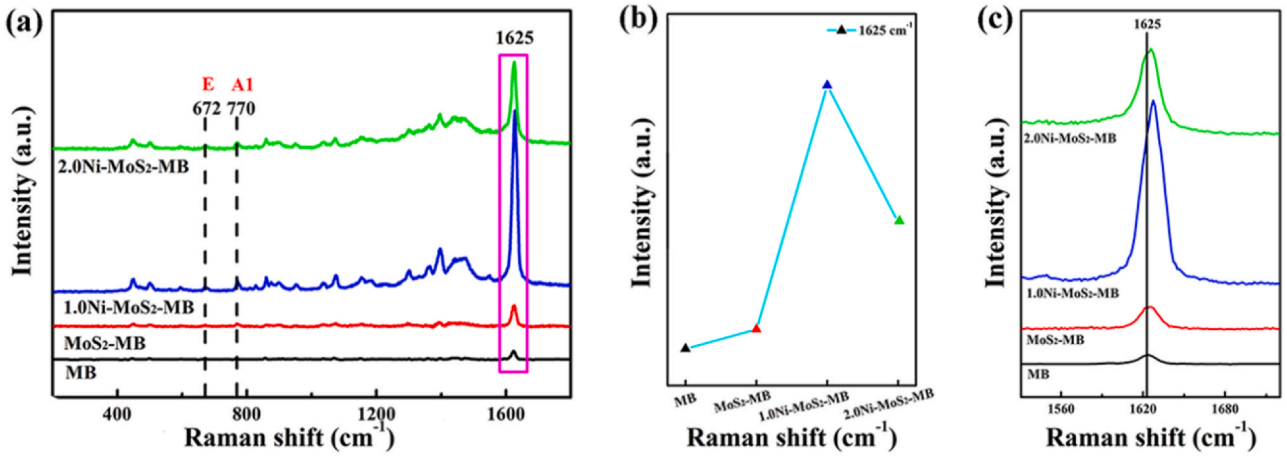

Fig. 5. (a) SERS spectra of MB molecules on four different substrates: 2.0Ni–MoS_2 NFs substrates, 1.0Ni-MoS_2 NFs substrates, MoS_2 NFs substrates and MB powders; (b) 1625 cm^{-1} Raman intensity of MB molecules adsorbed on different SERS-active substrates; (c) SERS spectra in the range of 1500–1700 cm^{-1}.

Where I_{ntsm} is the intensity of the Raman peak in the non-totally symmetric mode, and I_{tsm} is the intensity of the Raman peak in the totally symmetric mode. To test the ρ_{CT} in the SERS system, it is necessary to select a Raman peak that is less affected by the nearby peaks. Here, the 672 cm^{-1} non-totally symmetric mode and the 770 cm^{-1} totally symmetric mode have been selected [61]. Obviously, the non-totally symmetric Raman peak at 672 cm^{-1} has a stronger intensity. The calculation results show that ρ_{CT} is only about 43%. This result proves the role of CT in the SERS system.

At the same time, the interface dipole-dipole interaction between 1.0 Ni-MoS_2 NFs and MB molecules leads to the related perturbation of MB molecules, which further increases the Raman signal of MB molecules [62]. S atom is located on the layered surface and connected with Mo atom in the layer through covalent bond in the layered structure of MoS_2 NFs. There is a polar co-valent bond of Mo-S on the surface perpendicular to molybdenum disulfide. So MoS_2 NFs and MB molecules have a dipole-dipole interaction at the interface. But because of the symmetry in MoS_2 NFs protocells, most polarities cancel each other out, so there is a weak dipole-dipole interaction between MoS_2 NFs and MB. However, when MoS_2 NFs is doped, Ni atoms replace Mo atoms, destroying the symmetrical structure of MoS_2 NFs, and forming Ni–S–Mo bonds in the crystal, thereby increasing the polarity of MoS_2 NFs. Therefore, the dipole-dipole interaction between 1.0Ni–MoS_2 NFs and MB molecules is stronger than pure MoS_2 NFs [51,62]. In addition, linear sweep voltammetry (LSV) and electrochemical impedance spectroscopy (EIS) are used to further study the properties of 1.0Ni–MoS_2. As shown in Fig. 6a and Fig. S4, under the same conditions, 1.0Ni–MoS_2 NFs has a larger current density, and the Tafel slope is 104 mV, which is much lower than pure MoS_2 NFs. In Fig. 6b, the semicircle represents the charge transfer resistance. Compared with pure MoS_2 NFs, 1.0Ni-MoS_2 NFs has a smaller charge transfer resistance, which shows that 1.0Ni-MoS_2 NFs has a stronger charge transfer process. This is due to the appearance of the 1 T phase, which increases the carrier concentration in MoS_2 NFs, improves the available electron density in the state near the HOMO and LUMO of the molecule, thereby enhancing the charge transfer interaction of 1.0Ni–MoS_2-MB system [62,63]. According to Fermi's Golden Rule, the possibility of an electronic conversion can be expressed:

$$\omega_{lk} = \frac{2\pi}{\hbar} g(E_k) |H'_{kl}|^2 \quad (5)$$

Where $g(E_k)$ is the density of electronic state, $|H'_{kl}|$ is the matrix element of the LUMO-HOMO transition. Among them, the interface dipole-dipole interaction will cause local correlation disturbances in MoS_2 NFs, which will increase the matrix element $|H'_{kl}|$ in Eq. (5). The above analysis shows that 1.0Ni-MoS_2 NFs has a high electron state density and the strong interface dipole-dipole interaction between 1.0Ni–MoS_2 NFs and MB molecules, which further increases the Raman signal of MB molecules [62].

As everyone knows that the EM enhancement mechanism originates from the local electric field produced by the surface plasma in metal particles collective oscillation. When semiconductors are used as substrates, for semiconductors of different shapes, its plasmon resonance can also change as observed in metals, which is due to Mie scattering [20]. Therefore, as the size of the semiconductor substrate particles increases, the electric field in the semiconductor micron or nanostructures also increases, which

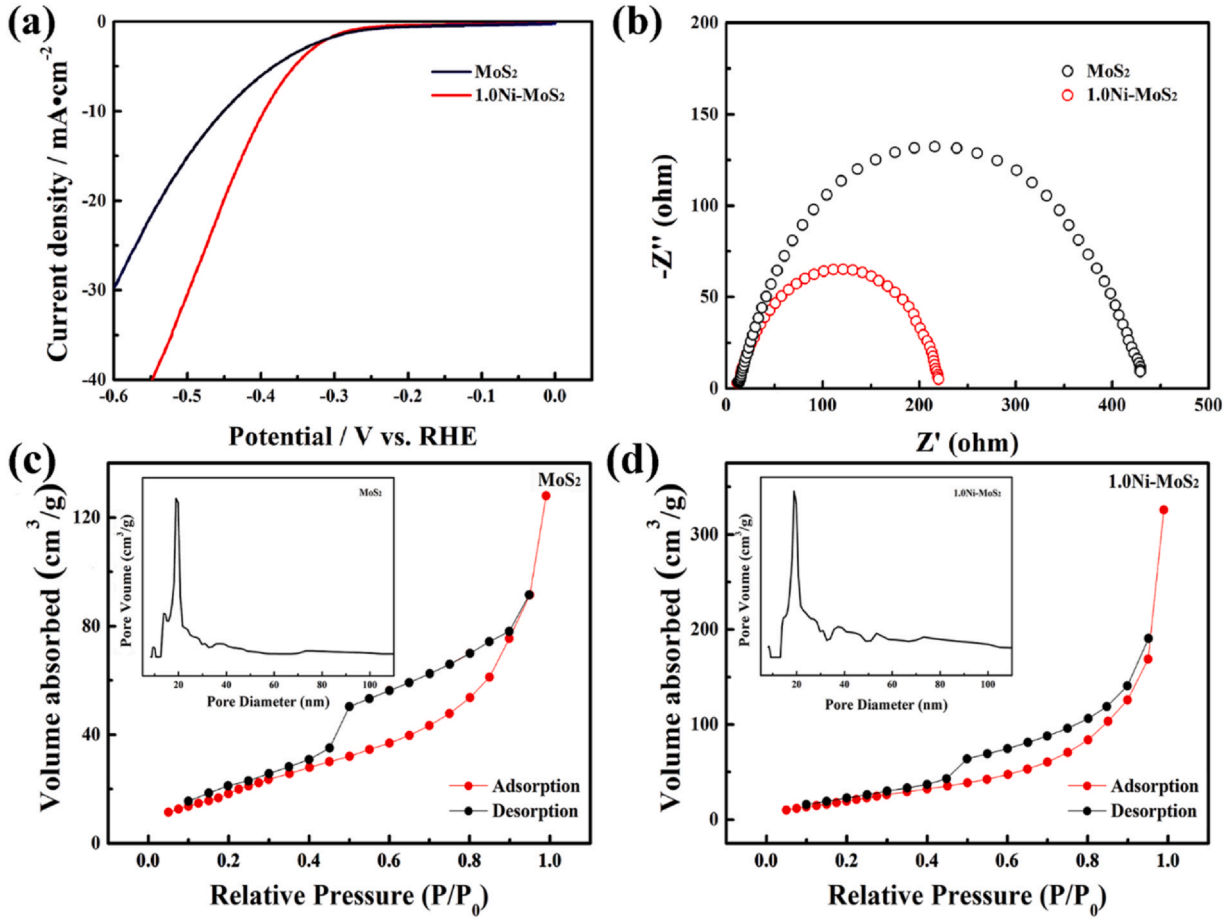

Fig. 6. (a) LSV curves of MoS_2 NFs and 1.0Ni–MoS_2 NFs; (b) Nyquist plots of MoS_2 NFs and 1.0Ni–MoS_2 NFs; (c) N_2 adsorption-desorption isotherm and pore size (inset) distribution of MoS_2 NFs; (d) N_2 adsorption desorption isotherm and pore size (inset) distribution of 1.0Ni–MoS_2 NFs.

promotes the improvement of Raman signals. From the SEM of 1.0Ni–MoS_2 NFs, it can be observed that the material agglomerates significantly, forming clusters with larger diameters, this is beneficial to the Raman signal enhancement of MB molecule in the 1.0 Ni–MoS_2–MB system. In addition, there are more metal 1 T phases in 1.0Ni–MoS_2 NFs. The original lattice is disturbed by Ni doping to induce electrons to compensate defects and increase free carriers, showing stronger LSPR perturbation, which is considered to be the electromagnetic enhancement of the SERS system [20].

In addition, the SERS activity of semiconductor nanomaterials is also determined by the specific surface area of the material and the strength of the adsorption performance. Through nitrogen adsorption experiments, the specific surface area of MoS_2 NFs and 1.0Ni-MoS_2 NFs were compared. The representative N_2 adsorption–desorption isotherms of MoS_2 and 1.0Ni-MoS_2 NFs are typical IV-shaped curves (Fig. 6c-d). The specific surface areas of the prepared MoS_2 NFs and 1.0Ni-MoS_2 NFs are 87.31 and 128.40 m^2/g, respectively, and the pore volume is 0.133 and 0.288 cm^3/g, respectively. It shows that the specific surface area of 1.0Ni-MoS_2 NFs is larger, which is more conducive to molecular adsorption. Fig. S4a-b shows water contact angle measurement on MoS_2 NFs and 1.0Ni-MoS_2 NFs. The contact angle of the original MoS_2 NFs is 63.0, and after doping, the contact angle of 1.0Ni-MoS_2 NFs is 49.5. It directly shows that doping can increase the hydrophilicity of MoS_2 NFs. The reason is that there is more hydrophilic 1 T MoS_2 on 1.0Ni-MoS_2 NFs, which promotes molecular absorption [41]. This enhanced hydrophilicity facilitates the diffusion of molecules to the surface of 1.0Ni–MoS_2 NFs and promotes the SERS performance of the material.

In summary, the high SERS activity of the 1.0Ni–MoS_2 NFs substrate is mainly the result of the combined effect of electromagnetic enhancement and chemical enhancement [64]. The chemical enhancement mainly comes from the charge transfer between MB molecule and 1.0Ni-MoS_2, and the dipole-dipole interaction between MB molecule and 1.0Ni-MoS_2 NFs interface. In addition, the strong adsorption capacity also provides more possibilities for charge transfer and interface dipole-dipole interaction.

2.4. SERS performance of 1.0Ni–MoS_2 NFs

High stability, repeatability and uniformity are essential parameters for an outstanding SERS substrate. Hence, while keeping the experimental conditions unchanged, the SERS spectra of MB are gathered to estimate these parameters of the 1.0Ni–MoS_2 NFs substrates. As shown in Fig. 7a, 30 points were randomly selected on the substrate to collect SERS spectra of 10^{-3} M MB. Fig. 7b shows the signal intensity distribution at 1625 cm^{-1}. The result implied that the 1.0Ni–MoS_2 NFs substrate exhibited outstanding reproducibility. This may be due to the uniform distribution of active sites on the substrate. In order to verify its stability, a substrate within 6 months was selected for SERS performance test. The result is shown in Fig. 7c, and no significant changes were observed. Therefore, the 1.0Ni–MoS_2 NFs substrate is stable. The recyclable detection performance of the 1.0Ni–MoS_2 NFs is tested with the concentration of 10^{-3} M for MB in Fig. 7d. The results showed that the substrate exhibited good sensitivity and recoverable stability in 5 cycles of testing.

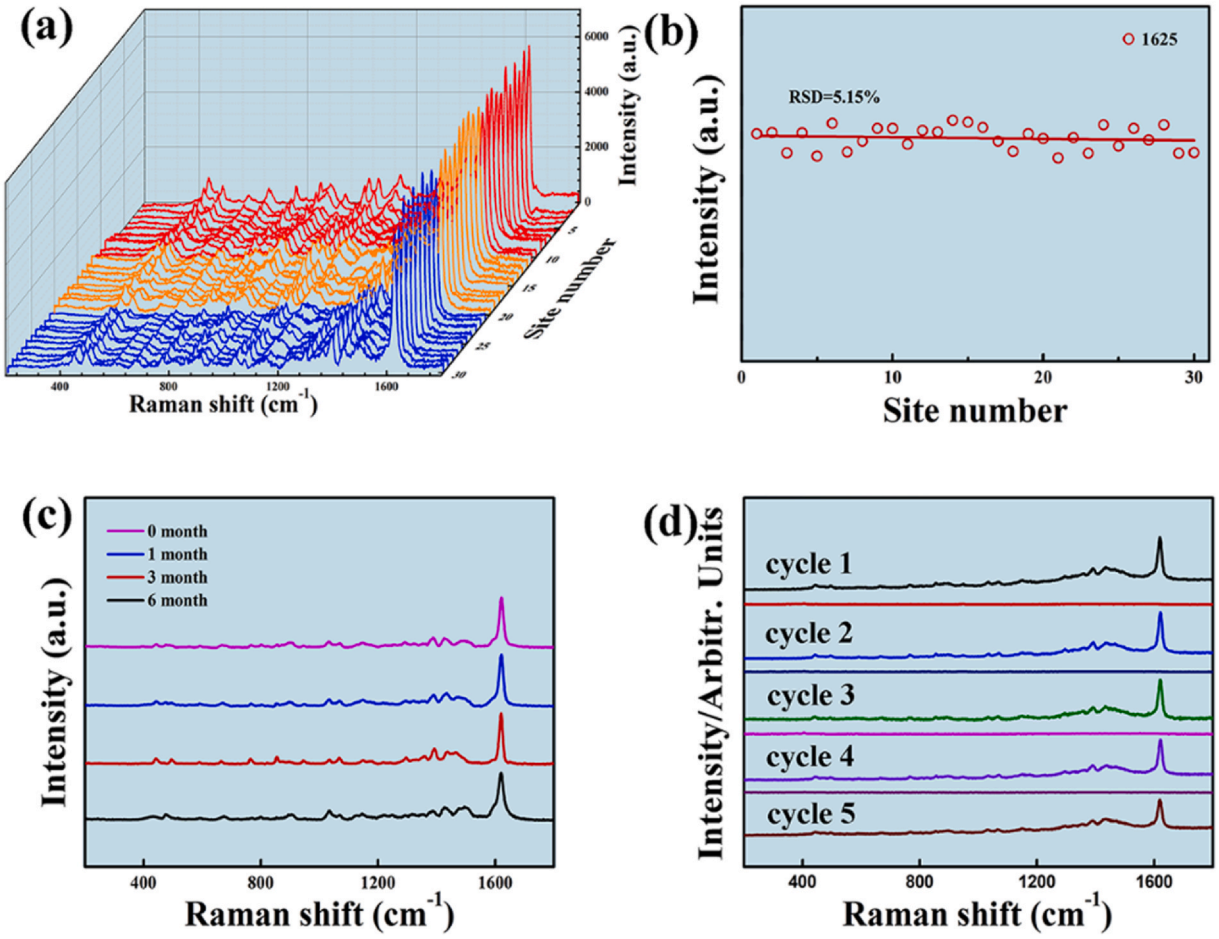

Fig. 7. (a) SERS spectrum of 10^{-3} M MB with 1.0Ni–MoS_2 NFs acquired from 30 random points; (b) the RSD result of the SERS peak intensity of MB at 1625 cm^{-1}; (c) SERS spectra of MB tested with 1.0Ni–MoS_2 NFs samples of stored different times; (d) SERS spectra of MB before and after self-cleaning test.

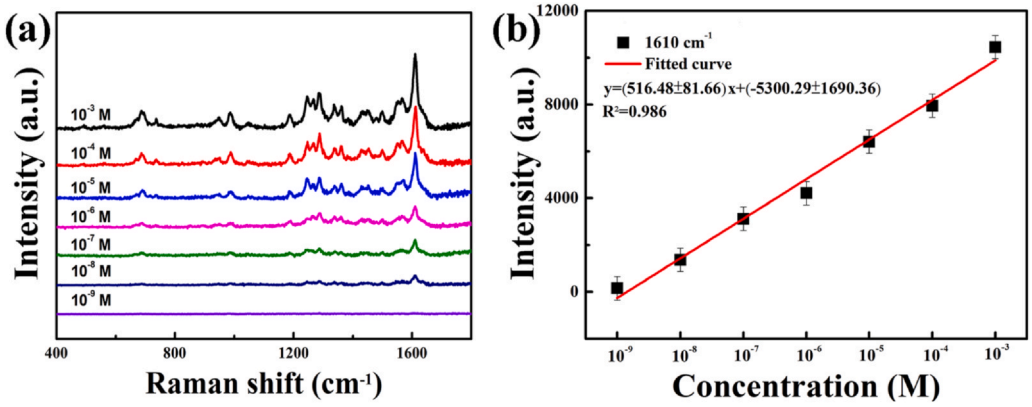

Fig. 8. (a) SERS spectra recorded from 1.0Ni–MoS_2 NFs substrate for bilirubin with different concentrations (10^{-3} to 10^{-8} M); (b) Plot of logarithmic Raman intensity at 1610 cm^{-1} versus logarithmic bilirubin concentration.

As a component of human blood, bilirubin is an important biological molecule. Its content in the organism reflects the health of the human body. When the bilirubin in the blood is low, it is easy to cause chronic kidneys, and too high content can easily cause problems such as liver cirrhosis [65,66]. Therefore, we use 1.0Ni-MoS_2 NFs substrates to further test the bilirubin in the serum. Fig. 8a shows the Raman signal of different concentration (10^{-3} to 10^{-8} M) bilirubin molecules on 1.0Ni-MoS_2 NFs substrates. Bilirubin molecules show a wonderful SERS signal and achieved a minimum LOD of 1.0×10^{-7} M. The Raman spectrum of bilirubin is given in Fig. S5 and the Raman mode assignment of bilirubin is given in Supplementary Note 2. The Raman signal at 1612 cm^{-1} is chosen to prove the relationship between bilirubin concentration and SERS intensity. The logistic linear fitting curve (R^2 = 0.977) in Fig. 8b demonstrates to the excellent ability of quantitatively detecting bilirubin. Table S4 shows the detection limit of bilirubin by different analytical methods. The results show that the prepared 1.0Ni–MoS_2 NFs have high sensitivity, and the substrate can detect 10^{-7} M bilirubin. This is very rare for non-precious metal materials.

In order to explore the unknown application of 1.0Ni–MoS_2 NFs in the SERS field, we tested different target molecules, including thiram and cytochrome c which are typical representatives of pesticides and pigments in organisms. The preparation method is given in Supplementary Note 3. The Raman characteristic peaks of

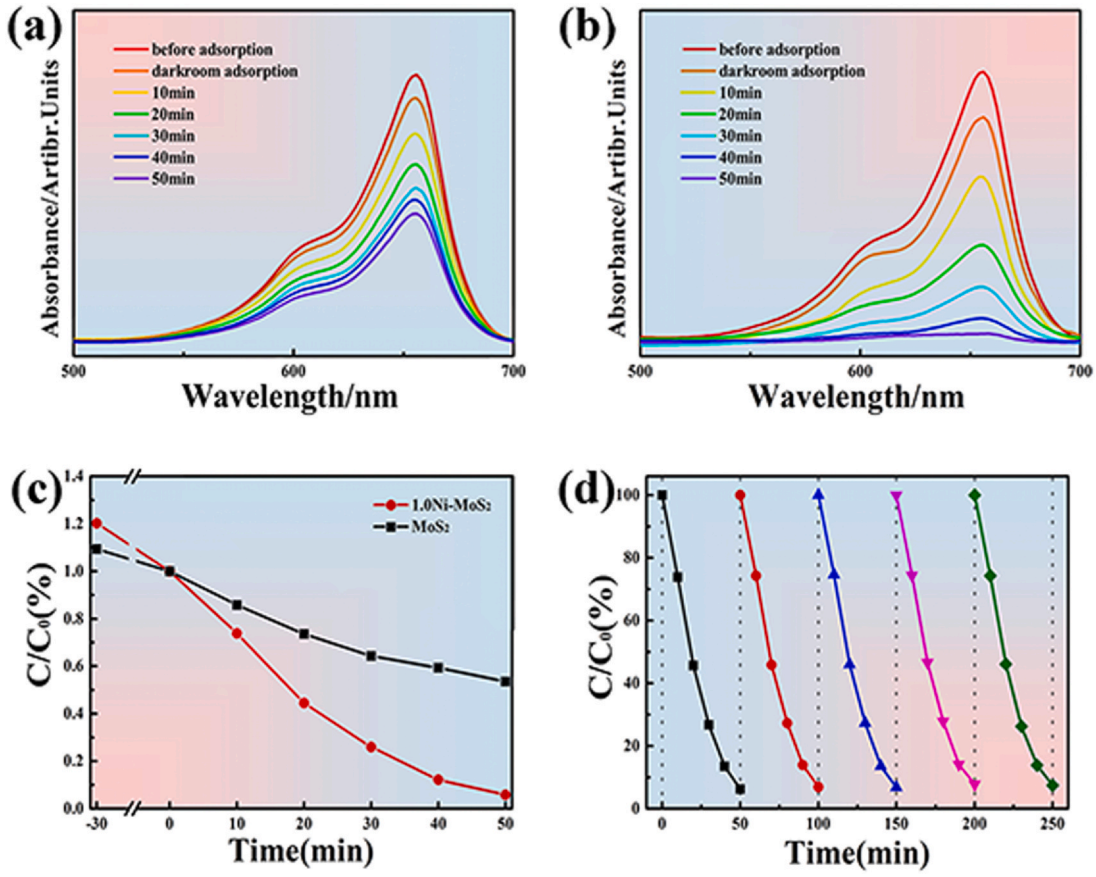

Fig. 9. (a) UV-Vis Absorption Spectra of MB Solution Catalyzed by MoS_2 NFs; (b) UV-Vis Absorption Spectra of MB Solution Catalyzed by 1.0Ni-MoS_2 NFs; (c) Variation of MB relative concentration (C/C_0) with irradiation time under different samples; (d) Reusability of 1.0Ni–MoS_2 NFs for degradation process of MB during the five cycles.

different target molecules are obtained in Fig S6, which are the same as the previous test results [67,68]. It shows that 1.0Ni–MoS_2 NFs as SERS substrate has the ability to detect different probe molecule and has good universality.

2.5. Photocatalytic activity of 1.0Ni–MoS_2 NFs

Through the above test, we found that 1.0Ni-MoS_2 NFs has a larger specific surface area, a stronger current density, and a smaller impedance. These not only promote the SERS of the material, but also play a key role in the catalytic performance of the material. Therefore, we also evaluated the photocatalytic activity of 1.0Ni-MoS_2 NFs. As shown in Fig. 9a-b, the degradation of MB by MoS_2 NFs and 1.0Ni–MoS_2 NFs preliminarily shows that 1.0Ni-MoS_2 NFs has better photocatalytic activity. Before light irradiation, a 30-minute darkroom adsorption experiment was carried out to ensure that the sample reached the adsorption-desorption equilibrium. As shown in Fig. 9c, we define the degradation efficiency of MB as C/C_0, where C is the concentration of MB solution in the degradation process, and C_0 is the concentration of MB solution after adsorption equilibrium. The results showed that the photocatalytic efficiencies of pure MoS_2 NFs and 1.0Ni-MoS_2 NFs are 46.5% and 94.23%, respectively, within 50 min. At the same time, MG and MO were also catalytically degraded, and their catalytic rates were 92.1% and 91.9% (Fig. S7). To better understand the degradation process, the kinetics is proved by the Langmuir-Hinshelwood equation:

$$\ln(C0/C) = kt \quad (8)$$

Where k is the reaction rate constant and t is the reaction time. The results show that the degradation reaction conforms to a typical first-order reaction (Fig. S8). In addition, in order to verify the repeatability of 1.0Ni–MoS_2 NFs, the sample was tested for 5 cycles. As shown in Fig. 9d, in the fifth cycle test, the MB degradation rate was 92.54%, indicating that 1.0Ni-MoS_2 NFs still has high catalytic activity. The above results indicate that 1.0Ni-MoS_2 NFs has good catalytic activity, which may be related to the large specific surface area, low resistance and strong polarity of 1.0Ni-MoS_2 NFs.

3. Conclusion

In summary, a simple one-step hydrothermal method successfully obtained 1.0Ni–MoS_2 NFs containing more defects and 1 T phase. The enhancement mechanism of the 1.0Ni–MoS_2–MB system is studied by MB as the probe molecule. The experimental analysis results show that Ni doping destroys the structure of MoS_2 NFs and induces defects, increases the electronic density of MoS_2 NFs, and increases the 1 T phase in MoS_2 NFs, which is beneficial to enhance the adsorption capacity of MoS_2 NFs to foreign molecules and improving the charge transfer between MoS_2 NFs and foreign molecules. At the same time, 1.0Ni-MoS_2 NFs as a SERS substrate has high reproducibility and stability. And 1.0Ni–MoS_2 NFs, as a non-precious metal material, shows good sensitive in the detection of bilirubin. Therefore, 1.0Ni–MoS_2 NFs has sufficient potential as a potential SERS active substrate for detecting trace targets. In addition, the photocatalytic activity of 1.0Ni–MoS_2 NFs has also been greatly improved. This study shows that Ni doping not only contributes to the improvement of SERS performance, but also enhances the catalytic activity of MoS_2 NFs. This is conducive to the detection and degradation of dyes and other harmful substances. In addition, the enhancement mechanism of the 1.0Ni–MoS_2–MB system is analyzed in detail, which provides a reference for the SERS mechanism of semiconductor substrates.

CRediT authorship contribution statement

R.S. and M.G. put forward ideas and explore the project; Y.Q. conducted the experiment; All samples were prepared by S.Y., M.H. and R.S.; S.Y. and J.Y. participated in the discussion. All the authors participated in data analysis and manuscript writing.

Declaration of Competing Interest

The authors declare that they have no known competing financial interests or personal relationships that could have appeared to influence the work reported in this paper.

Acknowledgements

This work was supported by the National Natural Science Foundation of China (No. 61675090, 21776110 and 21676115); National Youth Program Foundation of China (No. 61405072 and 61704065); the Program for the Development of Science and Technology Jilin Province (Grant Numbers 20200301043RQ, 20200201022JC, 20190103002JH and 20180520179JH, and 20180520179JH); the Thirteenth Five-Year Program for Science and Technology of Education Department of Jilin Province (Grant Numbers JJKH20200418KJ, JJKH20191018KJ, JJKH20191022KJ and JJKH20190550KJ).

Appendix A. Supporting information

Supplementary data associated with this article can be found in the online version at doi:10.1016/j.jallcom.2021.161268.

References

[1] J. Langer, D. Jimenez de Aberasturi, J. Aizpurua, R.A. Alvarez-Puebla, B. Auguie, J.J. Baumberg, G.C. Bazan, S.E.J. Bell, A. Boisen, A.G. Brolo, J. Choo, D. Cialla-May, V. Deckert, L. Fabris, K. Faulds, F.J. Garcia de Abajo, R. Goodacre, D. Graham, A.J. Haes, C.L. Haynes, C. Huck, T. Itoh, M. Kall, J. Kneipp, N.A. Kotov, H. Kuang, E.C. Le, Ru Lee H.K., J.F. Li, X.Y. Ling, S.A. Maier, T. Mayerhofer, M. Moskovits, K. Murakoshi, J.M. Nam, S. Nie, Y. Ozaki, I. Pastoriza-Santos, J. Perez-Juste, J. Popp, A. Pucci, S. Reich, B. Ren, G.C. Schatz, T. Shegai, S. Schlucker, L.L. Tay, K.G. Thomas, Z.Q. Tian, R.P. Van Duyne, T. Vo-Dinh, Y. Wang, K.A. Willets, C. Xu, H. Xu, Y. Xu, Y.S. Yamamoto, B. Zhao, L.M. Liz-Marzan, Present and future of surface-enhanced Raman scattering, ACS Nano 14 (2020) 28–117.
[2] Y. Ye, C. Chen, W. Li, X. Guo, H. Yang, H. Guan, H. Bai, W. Liu, G. Xi, Highly sensitive W18O49 mesocrystal raman scattering substrate with large-area signal uniformity, Anal. Chem. 93 (2021) 3138–3145.
[3] Z. Wang, S. Zong, L. Wu, D. Zhu, Y. Cui, SERS-activated platforms for immunoassay: probes, encoding methods, and applications, Chem. Rev. 117 (2017) 7910–7963.
[4] B. Sharma, R.R. Frontiera, A.-I. Henry, E. Ringe, R.P.V. Duyne, SERS: materials, applications, and the future, Mater. Today 15 (2012) 16–25.
[5] B. Hao, X. Bu, J. Wu, Y. Ding, L. Zhang, B. Zhao, Y. Tian, Determination of Hg2+ in water based on acriflavine functionalized AgNPs by SERS, Microchem. J. 155 (2020) 104736.
[6] J. Singh, Rishikesh, S. Kumar, R.K. Soni, Synthesis of 3D-MoS2 nanoflowers with tunable surface area for the application in photocatalysis and SERS based sensing, J. Alloys Compd. 849 (2020) 156502.
[7] D. Han, J. Yao, Y. Quan, M. Gao, J. Yang, Plasmon-coupled charge transfer in FSZA core-shell microspheres with high SERS activity and pesticide detection, Sci. Rep. 9 (2019) 13876.
[8] C. Zong, M. Xu, L.-J. Xu, T. Wei, X. Ma, X.-S. Zheng, R. Hu, B. Ren, Surface-enhanced raman spectroscopy for bioanalysis: reliability and challenges, Chem. Rev. 118 (2018) 4946–4980.
[9] T. Man, W. Lai, M. Xiao, X. Wang, A.R. Chandrasekaran, H. Pei, L. Li, A versatile biomolecular detection platform based on photo-induced enhanced Raman spectroscopy, Biosens. Bioelectron. 147 (2020) 111742.
[10] Y. Quan, J. Yao, S. Yang, L. Chen, J. Li, Y. Liu, J. Lang, H. Shen, Y. Wang, Y. Wang, J. Yang, M. Gao, ZnO nanoparticles on MoS2 microflowers for ultrasensitive SERS detection of bisphenol A, Mikrochim. Acta 186 (2019) 593.
[11] D. Zhang, H. You, L. Yuan, R. Hao, T. Li, J. Fang, Hydrophobic slippery surface-based surface-enhanced Raman spectroscopy platform for ultrasensitive detection in food safety applications, Anal. Chem. 91 (2019) 4687–4695.
[12] H. Cui, S. Li, S. Deng, H. Chen, C. Wang, Flexible, transparent, and free-standing silicon nanowire SERS platform for in situ food inspection, ACS Sens 2 (2017) 386–393.
[13] N.R. Barveen, T.-J. Wang, Y.-H. Chang, Z. Yuan-Liu, Ultrasensitive and reusable SERS probe for the detection of synthetic dyes in food industry through hybrid flower-shaped ZnO@Ag nanostructures, J. Alloys Compd. 861 (2021) 157952.

[14] Y. Quan, J. Yao, S. Yang, L. Chen, Y. Liu, J. Lang, H. Zeng, J. Yang, M. Gao, Detect, remove and re-use: sensing and degradation pesticides via 3D tilted ZMRs/Ag arrays, J. Hazard Mater. 391 (2020) 122222.

[15] J. Yao, Y. Quan, M. Gao, R. Gao, L. Chen, Y. Liu, J. Lang, H. Shen, Y. Zhang, L. Yang, J. Yang, AgNPs decorated Mg-doped ZnO heterostructure with dramatic SERS activity for trace detection of food contaminants, J. Mater. Chem. C 7 (2019) 8199–8208.

[16] S. Schlücker, Surface-enhanced raman spectroscopy: concepts and chemical applications, Angew. Chem. Int. Ed. 53 (2014) 4756–4795.

[17] J.F. Li, Y.J. Zhang, S.Y. Ding, R. Panneerselvam, Z.Q. Tian, Core-shell nanoparticle-enhanced Raman spectroscopy, Chem. Rev. 117 (2017) 5002–5069.

[18] W. Liao, K. Liu, Y. Chen, J. Hu, Y. Gan, Au–Ag bimetallic nanoparticles decorated silicon nanowires with fixed and dynamic hot spots for ultrasensitive 3D SERS sensing, J. Alloys Compd. 868 (2021) 159136.

[19] Z. Daxin, Y. Shuo, Z. Xin-Yuan, M. Ning, H. Bingbing, Z. Wenshi, C. Shaohua, L. Yang, Y. Jinghai, C. Lei, Damping resonance and refractive index effect on the layer-by-layer sputtering of Ag and Al2O3 on the polystyrene template, Spectrochim. Acta Part A Mol. Biomol. Spectrosc. 238 (2020) 118430.

[20] X.X. Han, W. Ji, B. Zhao, Y. Ozaki, Semiconductor-enhanced Raman scattering: active nanomaterials and applications, Nanoscale 9 (2017) 4847–4861.

[21] X.Y. Zhang, S. Yang, L. Yang, D. Zhang, Y. Sun, Z. Pang, J. Yang, L. Chen, Carrier dynamic monitoring of a pi-conjugated polymer: a surface-enhanced Raman scattering method, Chem. Commun. 56 (2020) 2779–2782.

[22] S. Cong, Y. Yuan, Z. Chen, J. Hou, M. Yang, Y. Su, Y. Zhang, L. Li, Q. Li, F. Geng, Z. Zhao, Noble metal-comparable SERS enhancement from semiconducting metal oxides by making oxygen vacancies, Nat. Commun. 6 (2015) 7800.

[23] S. Yang, J. Yao, Y. Quan, M. Hu, R. Su, M. Gao, D. Han, J. Yang, Monitoring the charge-transfer process in a Nd-doped semiconductor based on photoluminescence and SERS technology, Light Sci. Appl. 9 (2020) 117.

[24] S. Guo, Y. Zhang, S. Tang, B. Wang, Y. Wang, Y. Song, X. Xin, Y. Zhang, X. Li, Tuning interlayer spacing of MoS_2 for enhanced hydrogen evolution reaction, J. Alloys Compd. 864 (2021).

[25] Y. Xu, J. Qu, Y. Li, M. Zhu, Y. Liu, R. Zheng, J.M. Cairney, W. Li, Bridging metal-ion induced vertical growth of MoS_2 and overall fast electron transfer in $(C, P)_3N_4$–M (Ni^{2+}, Co^{2+})–MoS_2 electrocatalyst for efficient hydrogen evolution reaction, Sustain. Mater. Technol. 25 (2020) e00172.

[26] H. Park, N. Liu, B.H. Kim, S.H. Kwon, S. Baek, S. Kim, H.K. Lee, Y.J. Yoon, S. Kim, Exceptionally uniform and scalable multilayer MoS_2 phototransistor array based on large-scale MoS_2 grown by RF sputtering, electron beam irradiation, and sulfurization, ACS Appl. Mater. Interfaces 12 (2020) 20645–20652.

[27] A. Nourbakhsh, A. Zubair, R.N. Sajjad, K.G.A. Tavakkoli, W. Chen, S. Fang, X. Ling, J. Kong, M.S. Dresselhaus, E. Kaxiras, K.K. Berggren, D. Antoniadis, T. Palacios, MoS_2 field-effect transistor with Sub-10 nm channel length, Nano Lett. 16 (2016) 7798–7806.

[28] J.S. Ko, D.H. Shin, W.J. Lee, C.W. Jang, S. Kim, S.-H. Choi, All-two-dimensional semitransparent and flexible photodetectors employing graphene/MoS_2/graphene vertical heterostructures, J. Alloys Compd. 864 (2021) 158118.

[29] J.-D. Yi, T.-T. Liu, Y.-B. Huang, R. Cao, Solid-state synthesis of MoS_2 nanorod from molybdenum-organic framework for efficient hydrogen evolution reaction, Sci. China Mater. 59 (2016) 1051–1061.

[30] S. Liu, X. Zhang, J. Zhang, Z. Lei, X. Liang, B. Chen, MoS_2 with tunable surface structure directed by thiophene adsorption toward HDS and HER, Sci. China Mater. 59 (2016) 1051–1061.

[31] G. Eda, H. Yamaguchi, D. Voiry, T. Fujita, M. Chen, M. Chhowalla, Photoluminescence from chemically exfoliated MoS_2, Nano Lett. 11 (2011) 5111–5116.

[32] W. Ding, L. Hu, J. Dai, X. Tang, R. Wei, Z. Sheng, C. Liang, D. Shao, W. Song, Q. Liu, M. Chen, X. Zhu, S. Chou, X. Zhu, Q. Chen, Y. Sun, S.X. Dou, Highly ambient-stable 1T-MoS_2 and 1T-WS_2 by hydrothermal synthesis under high magnetic fields, ACS Nano 13 (2019) 1694–1702.

[33] Z. Qian, L. Jiao, L. Xie, Phase engineering of two-dimensional transition metal dichalcogenides, Chin. J. Chem. 38 (2020) 753–760.

[34] E. Er, H.-L. Hou, A. Criado, J. Langer, M. Möller, N. Erk, L.M. Liz-Marzán, M. Prato, High-yield preparation of exfoliated 1T-MoS_2 with SERS activity, Chem. Mater. 31 (2019) 5725–5734.

[35] K. Ueno, H. Misawa, Surface plasmon-enhanced photochemical reactions, J. Photo Photo C 15 (2013) 31–52.

[36] Y. Quan, J. Yao, Y. Sun, X. Qu, R. Su, M. Hu, L. Chen, Y. Liu, M. Gao, J. Yang, Enhanced semiconductor charge-transfer resonance: unprecedented oxygen bidirectional strategy, Sens. Actuators B Chem. 327 (2021) 128903.

[37] X. Liang, Y.S. Wang, T.T. You, X.J. Zhang, N. Yang, G.S. Wang, P.G. Yin, Interfacial synthesis of a three-dimensional hierarchical MoS_2–NS@Ag-NP nanocomposite as a SERS nanosensor for ultrasensitive thiram detection, Nanoscale 9 (2017) 8879–8888.

[38] V.P. Pham, G.Y. Yeom, Recent advances in doping of molybdenum disulfide: industrial applications and future prospects, Adv. Mater. 28 (2016) 9024–9059.

[39] M.I. Khan, M.S. Hasan, K.A. Bhatti, H. Rizvi, A. Wahab, S.-u Rehman, M.J. Afzal, A. Nazneen, M. Fiaz khan, A. Nazir, M. Iqbal, Effect of Ni doping on the structural, optical and photocatalytic activity of MoS_2, prepared by Hydrothermal method, Mater. Res. Express 7 (2020) 015061.

[40] C. Wang, Effect of Ni doping on electrocatalytic hydrogen evolution activity of MoS_2, Int J. Electrochem. Sci. 14 (2019) 11607–11615.

[41] X. Zheng, Z. Guo, G. Zhang, H. Li, J. Zhang, Q. Xu, Building a lateral/vertical ^1T–^2H MoS2/Au heterostructure for enhanced photoelectrocatalysis and surface enhanced Raman scattering, J. Mater. Chem. A 7 (2019) 19922–19928.

[42] Y.R. Girish, R. Biswas, M. De, Mixed-phase 2D-MoS_2 as an effective photocatalyst for selective aerobic oxidative coupling of amines under visible-light irradiation, Chem. Eur. J. 24 (2018) 13871–13878.

[43] R. Luo, M. Luo, Z. Wang, P. Liu, S. Song, X. Wang, M. Chen, The atomic origin of nickel-doping-induced catalytic enhancement in MoS_2 for electrochemical hydrogen production, Nanoscale 11 (2019) 7123–7128.

[44] D. Wang, X. Zhang, Y. Shen, Z. Wu, Ni-doped MoS_2 nanoparticles as highly active hydrogen evolution electrocatalysts, RSC Adv. 6 (2016) 16656–16661.

[45] X. Dai, K. Du, Z. Li, M. Liu, Y. Ma, H. Sun, X. Zhang, Y. Yang, Co-doped MoS2 nanosheets with the dominant CoMoS phase coated on carbon as an excellent electrocatalyst for hydrogen evolution, ACS Appl. Mater. Interfaces 7 (2015) 27242–27253.

[46] T. Dong, X. Zhang, P. Wang, H.-S. Chen, P. Yang, Formation of Ni-doped MoS_2 nanosheets on N-doped carbon nanotubes towards superior hydrogen evolution, Electrochim. Acta 338 (2020) 135885.

[47] Y. Jiang, D. Wang, Z. Pan, H. Ma, M. Li, J. Li, A. Zheng, G. Lv, Z. Tian, Microemulsion-mediated hydrothermal synthesis of flower-like MoS_2 nanomaterials with enhanced catalytic activities for anthracene hydrogenation, Front Chem. Sci. Eng. 12 (2017) 32–42.

[48] L.R.L. Ting, Y. Deng, L. Ma, Y.-J. Zhang, A.A. Peterson, B.S. Yeo, Catalytic activities of sulfur atoms in amorphous molybdenum sulfide for the electrochemical hydrogen evolution reaction, ACS Catal. 6 (2016) 861–867.

[49] L.R.L. Ting, Y. Deng, L. Ma, Y.-J. Zhang, A.A. Peterson, B.S. Yeo, Tremella-like Ni3S2/MnS with ultrathin nanosheets and abundant oxygen vacancies directly used for high speed overall water splitting, Appl. Catal. B Environ. 257 (2019).

[50] P. Cheng, K. Sun, Y.H. Hu, Memristive behavior and ideal memristor of 1T phase MoS_2 nanosheets, Nano Lett. 16 (2016) 572–576.

[51] M. Chen, B. Ji, Z. Dai, X. Du, B. He, G. Chen, D. Liu, S. Chen, K.H. Lo, S. Wang, B. Zhou, H. Pan, Vertically-aligned 1T/2H-MS_2 (M = Mo, W) nanosheets for surface-enhanced Raman scattering with long-term stability and large-scale uniformity, Appl. Surf. Sci. 527 (2020) 146769.

[52] S. Chen, F. Yang, Z. Cao, C. Yu, S. Wang, H. Zhong, Enhanced photocatalytic activity of molybdenum disulfide by compositing ZnAl–LDH, Colloids Surf. A Physicochem. Eng. Asp. 586 (2020) 124140.

[53] P. Zuo, L. Jiang, X. Li, P. Ran, B. Li, A. Song, M. Tian, T. Ma, B. Guo, L. Qu, Y. Lu, Enhancing charge transfer with foreign molecules through femtosecond laser induced MoS_2 defect sites for photoluminescence control and SERS enhancement, Nanoscale 11 (2019) 485–494.

[54] X. Chen, H. Li, S. Wang, M. Yang, Y. Qi, Biomolecule-assisted hydrothermal synthesis of molybdenum disulfide microspheres with nanorods, Mater. Lett. 66 (2012) 22–24.

[55] H.-U. Kim, H.Y. Kim, A. Kulkarni, C. Ahn, Y. Jin, Y. Kim, K.-N. Lee, M.-H. Lee, T. Kim, A sensitive electrochemical sensor for in vitro detection of parathyroid hormone based on a MoS_2-graphene composite, Sci. Rep. 6 (2016) 34587.

[56] A. Nazneen, M.I. Khan, M.A. Naeem, M. Atif, M. Iqbal, N. Yaqub, W.A. Farooq, Structural, morphological, optical, and photocatalytic properties of Ag-doped MoS2 nanoparticles, J. Mol. Struct. 1220 (2020) 128735.

[57] Z. Chang, X. Ju, P. Guo, X. Zhu, C. Liao, Y. Zong, X. Li, X. Zheng, Enhanced performance of supercapacitor electrode materials based on hierarchical hollow flowerlike HRGOs/Ni-doped MoS_2 composite, J. Alloys Compd. 824 (2020) 153873.

[58] B. Birmingham, Z. Liege, N. Larson, W. Lu, K.T. Park, H.W.H. Lee, D.V. Voronine, M.O. Scully, Z. Zhang, Probing interaction between individual submonolayer nanoislands and bulk MoS_2 using ambient TERS, J. Phys. Chem. C 122 (2018) 2753–2760.

[59] F. Pan, G. Zhou, L. Huang, W. Li, M. Lin, C. Liu, Interfacial potassium induced enhanced Raman spectroscopy for single-crystal TiO_2 nanowhisker, Chin. J. Chem. Eng. 28 (2020) 889–895.

[60] J.R. Lombardi, R.L. Birke, Theory of surface-enhanced Raman scattering in semiconductors, J. Phys. Chem. C 118 (2014) 11120–11130.

[61] H. Dizajghorbani Aghdam, S. Moemen Bellah, R. Malekfar, Surface-enhanced Raman scattering studies of Cu/Cu_2O Core-shell NPs obtained by laser ablation, Spectrochim. Acta A Mol. Biomol. Spectrosc. 223 (2019) 117379.

[62] X. Ling, W. Fang, Y.H. Lee, P.T. Araujo, X. Zhang, J.F. Rodriguez-Nieva, Y. Lin, J. Zhang, J. Kong, M.S. Dresselhaus, Raman enhancement effect on two-dimensional layered materials: graphene, h-BN and MoS_2, Nano Lett. 14 (2014) 3033–3040.

[63] X. Song, Y. Wang, F. Zhao, Q. Li, H.Q. Ta, M.H. Rummeli, C.G. Tully, Z. Li, W.J. Yin, L. Yang, K.B. Lee, J. Yang, I. Bozkurt, S. Liu, W. Zhang, M. Chhowalla, Plasmon-free surface-enhanced Raman spectroscopy using metallic 2D materials, ACS Nano 13 (2019) 8312–8319.

[64] J.R. Lombardi, R.L. Birke, A unified view of surface-enhanced raman scattering, J. Phys. Chem. C 112 (2008) 5605–5617.

[65] X. Luo, X. Zhao, G.Q. Wallace, M.H. Brunet, K.J. Wilkinson, P. Wu, C. Cai, C.G. Bazuin, J.F. Masson, Multiplexed SERS detection of microcystins with aptamer-driven core-satellite assemblies, ACS Appl. Mater. Interfaces 13 (2021) 6545–6556.

[66] X. Pan, L. Li, H. Lin, J. Tan, H. Wang, M. Liao, C. Chen, B. Shan, Y. Chen, M. Li, A graphene oxide-gold nanostar hybrid based-paper biosensor for label-free SERS detection of serum bilirubin for diagnosis of jaundice, Biosens. Bioelectron. 145 (2019) 111713.

[67] M. Chen, W. Luo, Q. Liu, N. Hao, Y. Zhu, M. Liu, L. Wang, H. Yang, X. Chen, Simultaneous in situ extraction and fabrication of surface-enhanced raman scattering substrate for reliable detection of thiram residue, Anal. Chem. 90 (2018) 13647–13654.

[68] L.L. Qu, D.W. Li, L.X. Qin, J. Mu, J.S. Fossey, Y.T. Long, Selective and sensitive detection of intracellular $O_2^{\bullet-}$ using Au NPs/cytochrome c as SERS nanosensors, Anal. Chem. 85 (2013) 9549–9555.